Advance Access publication 2025 May 23

## First IFU observations of two GRB host galaxies at cosmic noon with JWST/NIRSpec

B. Topçu,<sup>1★</sup> P. Schady <sup>®</sup>, <sup>1</sup> S. Wuyts, <sup>1</sup> A. Inkenhaag <sup>®</sup>, <sup>1</sup> M. Arabsalmani, <sup>2,3</sup> H.-W. Chen, <sup>4</sup> L. Christensen, <sup>5,6</sup> V. D'Elia, <sup>7</sup> J. P. U. Fynbo, <sup>5,6</sup> K. E. Heintz <sup>6,5,6</sup> P. Jakobsson, <sup>8</sup> T. Laskar, <sup>9,10</sup> A. Levan, <sup>10</sup>

G. Pugliese , <sup>11</sup> A. Rossi , <sup>12</sup> R. L. C. Starling, <sup>13</sup> N. R. Tanvir, <sup>13</sup> P. Wiseman <sup>14</sup> and R. M. Yates

Accepted 2025 May 20. Received 2025 May 19; in original form 2025 March 4

#### **ABSTRACT**

Long gamma-ray bursts (GRBs) serve as powerful probes of distant galaxies. Their luminous afterglow pinpoints galaxies independent of luminosity, in contrast to most flux-limited surveys. Nevertheless, GRB-selected galaxy samples are not free from bias, instead tracing the conditions favoured by the progenitor stars. Characterizing the galaxy populations traced by GRBs is therefore important both to effectively use GRBs as probes as well as to place stronger constraints on the progenitor stars capable of forming long GRBs. Spatially resolved spectroscopic observations with integral field units (IFUs) provide valuable insights into the interstellar medium and stellar populations of GRB host galaxies. In this paper, we present results of the first two GRB host galaxies observed with the JWST/Near-Infrared Spectrograph IFU with a spatial resolution of  $\sim 1.6$  kpc; the hosts of GRB 150403A and GRB 050820A at redshifts  $z \sim 2.06$  and  $\sim 2.61$ , respectively. The data reveal two complex galaxy environments made up of two or more star-forming galaxies that are likely interacting given their small spatial separation (< 20 kpc) and line-of-sight velocity offsets (< 100 km s<sup>-1</sup>). The measured gas-phase metallicity, star formation rates (SFRs), and key diagnostic line ratios for each of the detected galaxies are overall consistent with the properties of other star-forming galaxies and GRB hosts at z > 2. However, differences in the SFR and metallicities of the interacting galaxies highlight the importance of spatially resolved observations in order to accurately characterize the galaxy properties traced by GRBs.

Key words: gamma-ray burst: general – gamma-ray-burst: individual: GRB 050820A and GRB 150403A – galaxies: abundances – galaxies: high-redshift – galaxies: ISM – galaxies: kinematics and dynamics.

#### 1 INTRODUCTION

Gamma-ray bursts (GRBs) are extremely luminous, short-lived outbursts of gamma rays that reach energies of  $10^{49}$ – $10^{54}$  erg (e.g., Berger et al. 2005; Zhang & Pe'er 2009), and were first detected serendipitously in the late 1960s (Klebesadel, Strong & Olson 1973). Observations reveal a bimodal distribution of GRB durations, leading to the classification of GRBs into two populations: long-duration GRBs with prompt  $\gamma$ -ray emission lasting longer than 2 s, and shortduration GRBs with emission shorter than 2 s. It is now widely accepted that long GRBs are associated with the core collapse of a massive star (Woosley & Bloom 2006), whereas short GRBs are formed from compact binary star mergers (Eichler et al. 1989; Narayan, Paczyński & Piran 1992; Abbott et al. 2017) (although see e.g. Rastinejad et al. 2022; Troja et al. 2022; Levan et al. 2024; Yang et al. 2024). Long GRBs are therefore powerful tracers of star formation since they select star-forming galaxies independent

<sup>&</sup>lt;sup>1</sup>Department of Physics, University of Bath, Clayerton Down, Bath BA2 7AY, UK

<sup>&</sup>lt;sup>2</sup>Excellence Cluster ORIGINS, Boltzmannstraße 2, D-85748 Garching, Germany

<sup>&</sup>lt;sup>3</sup>Ludwig-Maximilians-Universität, Schellingstraße 4, D-80799 München, Germany

<sup>&</sup>lt;sup>4</sup>Department of Astronomy & Astrophysics, The University of Chicago, 5640 S Ellis Ave., Chicago, IL 60637, USA

<sup>&</sup>lt;sup>5</sup>Niels Bohr Institute, University of Copenhagen, Jagtvej 128, DK-2200 N Copenhagen, Denmark

<sup>&</sup>lt;sup>6</sup>Cosmic Dawn Center (DAWN), Jagtvej 128, DK-2200 N Copenhagen, Denmark

<sup>&</sup>lt;sup>7</sup>Space Science Data Center (SSDC) – Agenzia Spaziale Italiana (ASI), I-00133 Roma, Italy

<sup>&</sup>lt;sup>8</sup>Centre for Astrophysics and Cosmology, Science Institute, University of Iceland, Dunhagi 5, 107 Reykjavik, Iceland

<sup>&</sup>lt;sup>9</sup>Department of Physics & Astronomy, University of Utah, Salt Lake City, UT 84112, USA

<sup>&</sup>lt;sup>10</sup>Department of Astrophysics/IMAPP, Radboud University, NL-6525 AJ Nijmegen, the Netherlands

<sup>11</sup> Anton Pannekoek Institute for Astronomy, University of Amsterdam, PO Box 94249, NL-1090GE Amsterdam, the Netherlands

<sup>&</sup>lt;sup>12</sup>INAF – Osservatorio di Astrofisica e Scienza dello Spazio, Via Piero Gobetti 93/3, I-40129 Bologna, Italy

<sup>&</sup>lt;sup>13</sup>School of Physics and Astronomy, University of Leicester, University Road, Leicester LE1 7RH, UK

<sup>&</sup>lt;sup>14</sup>School of Physics and Astronomy, University of Southampton, Southampton SO17 1BJ, UK

<sup>&</sup>lt;sup>15</sup>Centre for Astrophysics Research, University of Hertfordshire, Hatfield AL10 9AB, UK

<sup>\*</sup> E-mail: bt434@bath.ac.uk

of galaxy luminosity (e.g. Berger et al. 2003; Le Floc'h et al. 2003; Christensen, Hjorth & Gorosabel 2004; Kistler et al. 2009; Savaglio, Glazebrook & Le Borgne 2009), and can be detected out to very high redshifts (e.g, Greiner et al. 2009; Salvaterra et al. 2009; Tanvir et al. 2009). The successful, long GRB 'collapsar' model (Woosley 1993) nevertheless predicts a cap on the metallicity of the progenitor star (<  $0.3\,Z_\odot$ ), which would introduce selection effects in GRB-selected galaxy samples. Characterizing the properties of long GRB host galaxies is therefore not only important to test key predictions from GRB progenitor models, but it is also an essential step in order to understand the galaxy properties that are traced by long GRBs.

With a handful of exceptions (e.g. Rossi et al. 2014; Levan et al. 2023), long GRBs are found in low-luminosity, star-forming, lowmass galaxies (e.g. Le Floc'h et al. 2003; Fruchter et al. 2006; Kelly, Kirshner & Pahre 2008; Savaglio et al. 2009; Svensson et al. 2010; Li et al. 2011; Perley et al. 2016), with a preference for lower metallicity environments (e.g. Le Floc'h et al. 2003; Tanvir et al. 2004; Savaglio et al. 2009; Levesque et al. 2010a, b; Graham & Fruchter 2013; Krühler et al. 2015; Graham & Fruchter 2017), in agreement with the expectations of the collapsar model. The metallicity drop off, however, does not appear as a sharp cut-off, and a notable fraction of long GRBs have been found to reside within more massive, chemically enriched, and dusty galaxies (e.g. Fruchter et al. 2006; Krühler et al. 2011; Rossi et al. 2012; Perley et al. 2016; Tanga et al. 2018). Any metallicity bias should also become less important at higher redshift, when the Universe was less chemically enriched. However, due to the increasing difficulty in obtaining good quality spectra to measure the metallicity of GRB host galaxies at z > 2 (e.g. Krühler et al. 2015), it remains unclear at what redshift long GRBs are no longer biased tracers of star formation.

In addition to long GRBs showing a preference for low-metallicity environments, high spatial resolution Hubble Space Telescope (HST) observations reveal a strong tendency for long GRB host galaxies to exhibit irregular morphologies (Fruchter et al. 2006), with a significant fraction appearing to be interacting or merging systems (Conselice et al. 2005; Wainwright, Berger & Penprase 2007). Complementary to HST observations, H I 21 cm emission-line studies have identified GRB hosts with clear signs of interactions (e.g. Arabsalmani et al. 2015, 2019, 2022). Additionally, the detection of multiple absorbers along the line of sight in optical afterglow spectra at close velocity offsets from the GRB (e.g. Savaglio et al. 2002, 2012; Klose et al. 2004; Ferrero et al. 2009; Page et al. 2009) provides further indication that interaction may be a common feature of long GRB host galaxies, especially at z > 2. A possible reason for this is that galaxy interactions may trigger a starburst episode, leading to a rise in the formation of massive stars and thus in the likelihood of a long GRB event (Somerville, Primack & Faber 2001; López-Sánchez & Esteban 2009; Teyssier, Chapon & Bournaud 2010). Such merger interactions can also induce gas instabilities that funnel low-metallicity gas into central regions of galaxies, causing a starburst in the less enriched gas compared to the overall host galaxy interstellar medium (ISM). This combination of elevated star formation rates (SFRs) and low metallicities may create particularly favourable conditions for long GRB production.

With integral field unit (IFU) instruments such as the Visible Multi Object Spectrograph (LeFevre et al. 2003) and the Multi Unit Spectroscopic Explorer (MUSE; Bacon et al. 2010), it has been possible to obtain spatially resolved spectroscopic observations of GRB host galaxies, where both galaxy morphology and spectral properties can be studied (e.g. Christensen et al. 2008; Izzo et al. 2017; Krühler et al. 2017; Tanga et al. 2018; Thöne et al. 2024). The combined sensitivity, large field of view and high spatial resolution

(0.2 arcsec in wide-field mode) of MUSE has made it possible, in some cases, to study the stellar population at the GRB site, revealing metal poor H II regions, with ages < 10 Myr, implying massive long GRB progenitors (>  $20\,M_\odot$ ), in line with expectations of the collapsar model (although see GRB 111005A; Tanga et al. 2018). While valuable for studying nearby GRB host galaxies, the spectral coverage of MUSE (0.465–0.93  $\mu m$ ) limits the access to key diagnostic nebular lines for more distant galaxies, with [O III]  $\lambda5007$  and H $\alpha$  no longer being accessible at  $z\gtrsim1.0$ .

The unprecedented sensitivity and spectral range of the *JWST* has now significantly extended the redshift out to which sensitive and spatially resolved spectroscopic observations are available with the Near-Infrared Spectrograph (NIRSpec, Böker et al. 2022; Ferruit et al. 2022; Jakobsen et al. 2022). The operational wavelength range of NIRSpec is  $0.6-5.3~\mu m$ , providing access to strong optical line emission including  $H\alpha$  out to  $z\sim7$ .

Here, we present the results from JWST NIRSpec integral field spectrograph (IFS; Jakobsen et al. 2022) observations of the host galaxies of the two long GRBs, GRB 050820A and GRB 150403A at redshifts  $z \sim 2.65$  and  $\sim 2.06$ , respectively. These data were included in Schady et al. (2024) as part of a larger spectroscopic sample of GRB host galaxies at  $z \gtrsim 2$  (mostly spatially unresolved) that focused on the relation between GRB afterglow absorption and host galaxy emission-line metallicities. In this work, we present a more detailed analysis of the spatially resolved emission-line properties of the two targets, focusing on the dynamical properties and presenting a comparison with previously studied samples of long GRB host galaxies and high-redshift star-forming galaxies. In Section 2, we provide details on the NIRSpec observations and describe our data analysis in Section 3. In Section 4, we present our results on the kinematics and emission-line properties of the two galaxies, and in Section 5, we discuss the implications of our results and compare the two galaxies to a larger sample of z > 2 long GRB host galaxies and to the general star-forming galaxy population. Finally, we provide our conclusions in Section 6. All uncertainties are given as  $1\sigma$  unless otherwise stated and we assume a standard Lambda-cold dark matter cosmology with  $\Omega_M = 0.31$ ,  $\Omega_{\Lambda} = 0.69$ , and  $H_0 = 67.8$  km s<sup>-1</sup> Mpc<sup>-1</sup> (Planck Collaboration XIII 2016).

#### 2 OBSERVATIONS

The host galaxies of GRB 050820A and GRB 150403A were both part of a larger GRB host galaxy sample observed during a cycle-1 JWST/NIRSpec program (ID 2344; Schady et al. 2024). They were the only two galaxies in the sample to be observed using the IFS, prompted by the extended emission seen in pre-existing imaging of GRB 050820A and GRB 150403A with HST (Chen 2012) and the GRB Optical and Near-infrared Detector (Greiner et al. 2008), respectively. The JWST NIRSpec observations provide spatially resolved spectroscopic information on pixel scales 0.1 arcsec over a 3 arcsec × 3 arcsec field of view. The IFS point spread function full width half-maximum (FWHM) is around 2 pixels wide, corresponding to a physical spatial resolution of  $\sim 1.6$  kpc for both host galaxies. Observations were taken using the G140M/F100LP and G235M/F170LP grating/filter combinations corresponding to a wavelength coverage of 1.0-1.9 and 1.7-3.2 µm, respectively, which at the redshift of the two host galaxies, covered all strong emission lines from  $[OII] \lambda\lambda 3726,3729$  to  $[SII] \lambda\lambda 6717,6731$ . The spectral resolution ranges from  $R\sim500$  to  $\sim1500$ , corresponding to a velocity width resolution of  $\sigma \sim 85-250 \text{ km s}^{-1}$ .

The reduced and calibrated 3D spectra were downloaded from the Mikulski Archive for Space Telescopes (MAST) Data Discovery

### 1846 *B. Topçu et al.*

Portal.<sup>1</sup> The data were reduced with version 11.17.2 of the CRDS file selection software, using context jwst\_1140.pmap, and were calibrated with version 1.11.4 of the calibration software. The reader is referred to Schady et al. (2024) for further details regarding the observations of the targets.

#### 3 DATA ANALYSIS

#### 3.1 Gaussian line fitting

For both targets, emission from H $\alpha$ , H $\beta$ , [O II]  $\lambda\lambda$ 3726, 3729, and  $[O III] \lambda\lambda 4959$ , 5007 are detected, but there is no significant emission at the position of  $[NII] \lambda\lambda6549$ , 6584 or  $[SII] \lambda\lambda6717$ , 6731. The galaxy continuum is not detected in either spectra. Line fluxes for each spaxel were measured from Gaussian fits to the emission lines. For greater constraint, the fits were performed simultaneously for H $\beta$ and  $[O III] \lambda\lambda 4959$ , 5007, with the peak positions of all three lines tied to a consistent redshift and keeping the velocity widths also tied. Additionally, the flux ratio of the [O III] λλ4959, 5007 doublet was fixed at 1:3, as per Osterbrock (1989). The velocity width and peak position of all other fitted lines were then fixed to be consistent with the best-fitting values from the H $\beta$  and [O III]  $\lambda\lambda4959$ , 5007 line fits. Although the  $[O II] \lambda \lambda 3726$ , 3729 doublet was not resolved, a double Gaussian was fit to the line, and the total flux was taken as the sum of the two profiles. In those cases, where the velocity width of λλ4959, 5007 was unresolved, the fitted FWHM was left as a free parameter in subsequent line fits. Although [N II] λ6584 was undetected in the observations in both galaxies, a flux upper limit was determined from simultaneous fits to H $\alpha$  and [N II]  $\lambda$ 6584, with the peak position and velocity width tied as described above. The flux upper limit was then determined from the best fit amplitude and  $1\sigma$  uncertainty at the position of [N II]  $\lambda 6584$ .

All line fluxes were corrected for Milky Way dust extinction using the Schlafly & Finkbeiner (2011) E(B-V) reddening maps, which gave  $E(B-V)=0.038\pm0.001$  for GRB 050820A and  $E(B-V)=0.047\pm0.001$  for GRB 150403A. The extinction correction was performed assuming a Cardelli, Clayton & Mathis (1989) dust extinction curve with an average total-to-selective dust extinction value  $R_V=3.08$ .

The host galaxy dust reddening was calculated from the  $\text{H}\alpha/\text{H}\beta$  Balmer decrement assuming an intrinsic ratio  $\text{H}\alpha/\text{H}\beta = 2.86$  (Osterbrock 1989) and using the average Small Magellanic Cloud dust law from Pei (1992) with  $R_V = 2.93$ . In some cases, the measured host galaxy E(B-V) was less than zero, which is not physical, and the E(B-V) was therefore set to zero when applying dust corrections.

#### 3.2 Emission-line fluxes

Surface brightness maps were created for all detected lines (H $\alpha$ , H $\beta$ , [O II]  $\lambda\lambda$ 3726, 3729, and [O III]  $\lambda\lambda$ 4959, 5007). As an example, in Figs 1 and 2 we show the [O III]  $\lambda$ 5007 surface brightness map for the two targets. In Fig. 1, we also include an *HST* image of GRB 050820A (left-hand panel), showing continuum emission in the *F*775*W* filter alongside our NIRSpec [O III]  $\lambda$ 5007 surface brightness map. The extended nature of the emission regions is apparent in both the *HST* image and the [O III]  $\lambda$ 5007 surface brightness map.

Note that the surface brightness maps represent a pixel-by-pixel analysis of the flux based on Gaussian fits to the corresponding line in that spaxel, whereas in Schady et al. (2024), the surface brightness

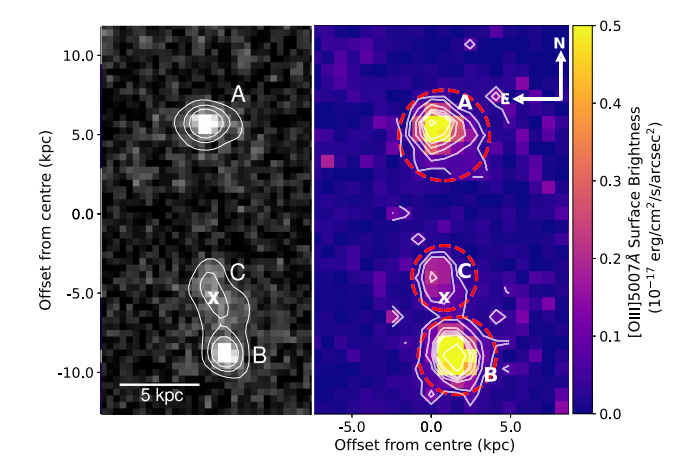
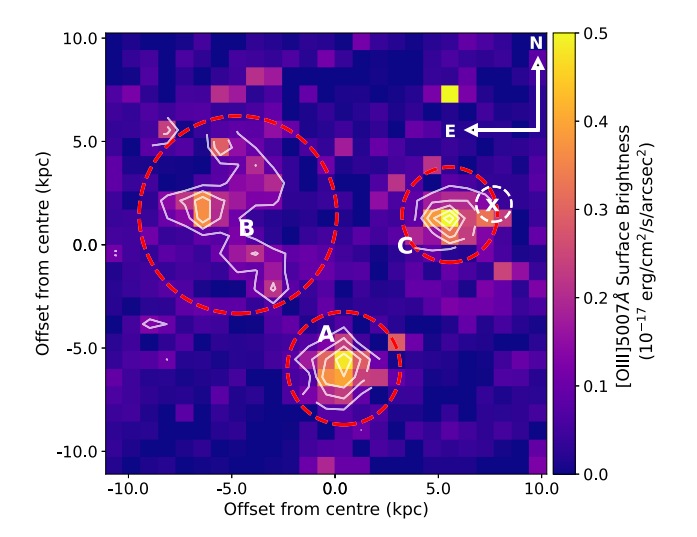


Figure 1. Image of the field of the host galaxy of GRB 050820A showing continuum emission at F775W observed with the HST/Advanced Camera for Surveys (ACS) (PID 10551; PI: S. Kulkarni) (left-hand panel) and [O III]  $\lambda 5007$  flux emission from our JWST/NIRspec data (right-hand panel). In both images, we label the star-forming components A and B identified in Chen (2012), as well as the fainter component C. The position of the GRB detected in early-epoch HST observations (Chen 2012) is indicated with an 'X'. The pixel scale of the HST and JWST images is 0.05 and 0.1 arcsec, respectively, and the uncertainty on the GRB position is within a couple of ACS pixels and a single NIRSpec pixel. For clarity, contours tracing the the F775W continuum at flux levels 0.6, 0.65, and 0.7  $\times 10^{-20}$  erg cm<sup>-2</sup> s<sup>-1</sup>, and the  $[O III] \lambda 5007$  surface brightness levels 0.05, 0.1, 0.2, 0.3, 0.4, 0.5, and 1.0  $\times 10^{-17}$  erg cm<sup>-2</sup> s<sup>-1</sup> arcsec<sup>-2</sup> are shown in white. Three dashed red circles in the right-hand panel indicate the sizes of the apertures used in our stacking analysis (see Section 3.2). Both images are oriented with north up and east to the left, and the physical scale is indicated in both panels.



**Figure 2.** [O III]  $\lambda$ 5007 surface brightness map of the host galaxy of GRB 150403A. Three star-forming components are labelled as A, B, and C. The position of the GRB afterglow is just west of component C indicated with an 'x'. The  $1\sigma$  uncertainty on the GRB position is indicated by the dashed circle. Some bright emission is observed to the north of C which is due to noise. Similarly, contours tracing the flux strength from 0.1 to  $0.5 \times 10^{-17}$  erg cm<sup>-2</sup> s<sup>-1</sup> arcsec<sup>-2</sup> are shown in white and the extraction regions used for stacking (see Section 3.2) are shown with dashed red circles. The pixel scale of the image is 0.1 arcsec.

<sup>&</sup>lt;sup>1</sup>https://mast.stsci.edu/portal/Mashup/Clients/Mast/Portal.html

**Table 1.** Total integrated and individual component emission-line fluxes for all detected lines in the host galaxies of GRB 050820A and GRB150403A. All line fluxes have been corrected for Milky Way dust extinction and are presented here without host galaxy reddening correction. The [N II]  $\lambda$ 6584 fluxes are reported as  $1\sigma$  upper limits.

GRB Host	z*em	Line flux $(10^{-17} \text{ erg cm}^{-2} \text{ s}^{-1})$						
	Cili	$_{ m Heta}$	Ηα	[Ο II] λλ3726, 3729	[O III] λ4959	[O III] λ5007	[N II] λ6584	
050820A								
Total integrated	2.6131	$2.85 \pm 0.11$	$10.49 \pm 0.26$	$5.13 \pm 0.22$	$6.33 \pm 0.17$	$18.66 \pm 0.19$	< 0.80	
Component A	2.6129	$1.14 \pm 0.08$	$4.67 \pm 0.13$	$1.76 \pm 0.12$	$2.43 \pm 0.11$	$7.17 \pm 0.15$	< 0.41	
Component B	2.6133	$1.50 \pm 0.05$	$4.83 \pm 0.27$	$2.38 \pm 0.07$	$3.35 \pm 0.08$	$9.87 \pm 0.11$	< 0.39	
Component C	2.6136	$0.42 \pm 0.04$	$1.44 \pm 0.21$	$0.98 \pm 0.06$	$0.68 \pm 0.10$	$2.00 \pm 0.12$	< 0.12	
150403A								
Total integrated	2.0563	$2.88 \pm 1.43$	$10.64 \pm 3.18$	$7.57 \pm 2.71$	$4.34 \pm 1.68$	$12.78 \pm 2.36$	< 2.96	
Component A	2.0564	$1.62 \pm 0.29$	$2.80 \pm 0.52$	$1.74 \pm 0.50$	$1.28 \pm 0.31$	$3.78 \pm 0.44$	< 0.19	
Component B	2.0562	$2.17 \pm 0.52$	$5.76 \pm 1.26$	$4.62 \pm 0.90$	$2.32 \pm 0.55$	$6.82 \pm 0.77$	< 0.69	
Component C	2.0571	$0.14 \pm 0.21$	$1.71 \pm 0.68$	$0.94 \pm 0.35$	$1.16\pm0.29$	$3.40 \pm 0.40$	< 0.16	

Note. \* In all cases, the measured redshift uncertainty is 0.0002.

**Table 2.** Table with NOX22  $R_{23}$  (Nakajima et al. 2022) and LMC24  $\hat{R}$  (Laseter et al. 2024) emission-line metallicities and Hα SFRs of the total integrated and individual components detected in the host galaxies of GRB 050820A and GRB 150403A. The measured host galaxy E(B-V) and  $\sigma$  values are also shown.

GRB host	Ŕ	$R_{23}$	$12 + \log(O/H)$		$SFR_{H\alpha}$	E(B-V)	σ
			NOX22 $R_{23}$	LMC24 R	$(M_{\odot} yr^{-1})$	(mag)	$({\rm km}\;{\rm s}^{-1})$
050820A							
Total integrated	$0.88 \pm 0.10$	$1.04 \pm 0.07$	$8.04 \pm 0.07$	$8.13 \pm 0.04$	$46 \pm 4$	$0.23 \pm 0.04$	$29 \pm 5$
Component A	$0.87 \pm 0.17$	$1.02 \pm 0.12$	$8.10 \pm 0.14$	$8.17 \pm 0.09$	$25 \pm 4$	$0.33 \pm 0.07$	$26 \pm 9$
Component B	$0.84 \pm 0.12$	$1.02 \pm 0.10$	$8.09 \pm 0.12$	$8.17 \pm 0.09$	$16 \pm 2$	$0.11 \pm 0.06$	$35 \pm 4$
Component C	$0.80 \pm 0.38$	$0.96 \pm 0.27$	$8.24 \pm 0.25$	$8.27 \pm 0.18$	$5.4 \pm 2.0$	$0.16 \pm 0.16$	< 98
150403A							
Total integrated	$0.81 \pm 1.22$	$0.96 \pm 0.87$	$8.40 \pm 0.42$	$8.39 \pm 0.31$	$24^{+27}_{-8}$	$0.20^{+0.50}_{-0.20}$	< 116
Component A	$0.34 \pm 0.13$	$0.62 \pm 0.09$	$8.60 \pm 0.08$	$8.57 \pm 0.05$	$4.2 \pm 0.8$	< 0.25*	$56 \pm 39$
Component B	$0.59 \pm 0.15$	$0.80 \pm 0.11$	$8.41 \pm 0.16$	$8.40 \pm 0.12$	$8.7 \pm 1.9$	< 0.83*	< 116
Component C	$1.86\pm2.31$	$1.77\pm1.71$	$< 8.79^{\dagger}$	$< 8.62^{\dagger}$	$39^{+76}_{-36}$	$1.35 \pm 0.94$	< 116

*Notes.* \* In these cases, the measured E(B-V) was less than zero, so we report the corresponding  $3\sigma$  upper limits and use E(B-V)=0 in our calculations. † The metallicity of GRB 150403A component C is reported with  $1\sigma$  upper limits due to the non-detection of H $\beta$  for this component.

maps were produced by collapsing a slice of the IFU data cube centred on the emission line of interest. As was done in Schady et al. (2024), we highlight three distinct emission regions in the two galaxies and label these 'A', 'B', and 'C'. In Schady et al. (2024), an additional emission region was seen to the left of component C in the [O III]  $\lambda$ 5007 map of the host galaxy of GRB 050820A, but this is no longer present with the improved NIRSpec data reduction used here, indicating that the feature was due to noise. Similar noise characteristics are observed to the north of component C in the surface brightness map of GRB 150403A in Fig. 2. These features are not present in other line maps and their spectral features resemble narrow spikes rather than Gaussian profiles. To help distinguish between regions of true line emission and noise, we show contours (white lines) in Figs 1 and 2 that trace the line flux strength. The flux map host galaxy dust corrections were applied to each of the three components separately, using the relevant E(B-V) measured from the corresponding Balmer decrement for each component, as reported in Table 2. A component-averaged dust correction was applied rather than computing the Balmer decrement on each individual spaxels in order to increase the signal-to-noise ratio (SNR) of the measured E(B-V), which was too low to construct an E(B-V) pixelated map for either observation.

In addition to the pixel-by-pixel analysis, we also measured the integrated fluxes for the individual star-forming components identified above within both targets and labelled in Figs 1 and 2. To do this, we stacked the spectra within a circular aperture centred on the region of interest and with a radius sufficiently large to ensure that the entire emission region was encompassed within the aperture, see dashed red circles in Figs 1 and 2. The apertures used had radii ranging from 0.25 to 0.6 arcsec. The stacking was performed by summing the spectra from individual spaxels within the aperture and propagating their respective uncertainties to obtain a single-stacked spectrum for each component. The line fluxes in the stacked spectra were then measured using Gaussian fits and we applied Milky Way and host galaxy dust corrections as previously described. In Figs A1 and A2, we show the Gaussian fits applied to the stacked spectra of the three components for both GRB 050820A and GRB 150403A.

We note that for the host galaxy of GRB 150403A, component B has two extended structures, and thus approximating this component by using a circular region results in a notable amount of background being included in the source aperture. To investigate the effect of the background noise on our measured line fluxes, we divided component B into three separate regions corresponding to the central circular emitting region and the two extended regions to the north-west and south-west. We then summed the line fluxes measured within each of these smaller regions. We found no significant difference in the measured line flux SNR between the two methods, and we therefore use the results from the single aperture method for further analysis. The Milky Way extinction corrected fluxes are reported in Table 1 for each component along with the redshifts corresponding to the best-fitting peak wavelength fitted to the [O III] λ5007 line. The

uncertainties on our redshift measurements include the NIRSpec wavelength calibration uncertainty, which is on the order of 0.8 Å.<sup>2</sup>

The fluxes we measure are generally in good agreement with those reported in Schady et al. (2024) within  $1\sigma$ , and larger differences can be explained by differences in the source extraction regions used for each component. The measured emission-line redshifts are consistent with the absorption line redshifts of 2.615 (Prochaska et al. 2007; Ledoux et al. 2009) and 2.057 (Selsing et al. 2019) measured from the afterglow spectra of GRB 050820A and GRB 150403A, respectively.

In Table 2, we give the measured host galaxy E(B-V) values for each component along with the measured intrinsic velocity dispersions,  $\sigma$ . We note that the measured  $\sigma$  values correspond to FWHM comparable to the NIRSpec line spread function (LSF) and the wavelength pixel scale. To quantify the impact of spectral resolution on our best-fitting line widths and peak wavelengths, we generated a Gaussian model on an oversampled wavelength grid, and then binned this to the wavelength scale of our observed spectra. We then re-fitted our spectra with this discretely sampled Gaussian model. Comparing the two cases, we found that the newly fitted line widths were 1.4 to 2.1 times narrower than the line widths measured from an unbinned Gaussian model, although the best-fitting peak wavelengths were unchanged within uncertainties. Consequently, we refrain from performing any analysis using the measured velocity widths, and merely report for completeness the (generally small or unresolved) velocity dispersions from the binned Gaussian model fits in Table 2. We considered any extra line broadening to be intrinsic only if it accounted for more than 10 per cent of the observed FWHM; otherwise, we report the sigma dispersion as an upper limit.

#### 4 RESULTS

#### 4.1 Kinematics

In order to study the relation between the multiple components detected in our IFS data we looked at the kinematics of each galaxy system. We created velocity field maps using the best-fitting peak wavelength to the  $[O\,III]\,\lambda5007$  line and converted this into rest-frame velocity space. Zero velocity was chosen to correspond to the redshift of the star-forming component hosting the GRB (component C in both cases). In order to reduce the noise present in the maps, a mask was applied to remove all spaxels with SNR < 2. The velocity maps for the two GRB host galaxies are shown in Fig. 3 where the contours corresponding to the three components identified in Figs 1 and 2 are overplotted in black.

In the data cube of GRB 050820A (Fig. 3, left-hand panel), component A stands out with having the largest velocity difference, with a peculiar velocity of  $-58 \pm 8$  km s<sup>-1</sup> relative to component C. Although this is not a significant velocity offset, when combined with the projected separation of  $\sim 8$  kpc from the other two components, the indication is that this is a separate but interacting galaxy in this system. In contrast, the spatial proximity of < 3 kpc and smaller velocity offset of  $-26 \pm 8$  km s<sup>-1</sup> between components B and C imply that these two components are interacting and possibly in the process of merging.

In the velocity map of GRB 150403A (Fig. 3, right-hand panel), both components A and B have velocity offsets relative to component C, indicating that they are blueshifted relative to component C. Based on redshifts determined from stacked spectra, we measure

peculiar velocities relative to component C of  $-68 \pm 15 \ \text{km s}^{-1}$  for component A and  $-96 \pm 15 \ \text{km s}^{-1}$  for component B. The projected separation between component C and the other two components ( $\sim 10 \ \text{kpc}$ ) along with the velocity offsets, suggests that component C, which we associate with the GRB, is a separate galaxy. Despite having a separation of  $\sim 20 \ \text{km s}^{-1}$  and sharing similar rotational velocity axes, components A and B also appear to be separate galaxies. If components A and B were part of a single galaxy, the observed velocity field in Fig. 3 (right-hand panel) would indicate rotation along the major axis, whereas galaxies are expected to rotate along the minor axis. None the less, the close proximity of all three components in velocity space implies that all three are gravitationally interacting.

#### 4.2 Star formation rates

The SFR of each component is estimated using the dust corrected integrated Hα fluxes (Kennicutt 1998) assuming a Chabrier (2003) initial mass function. The estimated values are reported in Table 2. For GRB 050820A, component C, which we associate with the GRB, has the lowest SFR. It is nevertheless still clearly a star-forming region, with an H $\alpha$  SFR of 5.4  $\pm$  2.0 M $_{\odot}$  yr $^{-1}$ . GRB 150403A also lies close to a star-forming region (component C), although SFR is more uncertain due to the undetected H $\beta$  line. The H $\alpha$  SFR of component C is  $39^{+76}_{-36}$  M<sub> $\odot$ </sub> yr<sup>-1</sup>. Here, the lower limit corresponds to the SFR inferred from the dust uncorrected  $H\alpha$  flux, corresponding to  $\sim 3 \text{ M}_{\odot} \text{ yr}^{-1}$ . From Fig. 2, we measure a projected separation between component C and the GRB position that is less than  $\sim$ 1.6kpc when accounting for the GRB positional uncertainty. This is consistent within  $1\sigma$  of the median offset measured in Blanchard, Berger & Fong (2016) and therefore suggests that while the GRB did not occur in the region of peak star formation, it is still likely associated with the nearby star-forming component.

#### 4.3 Emission-line metallicities

Multiple gas-phase metallicity line diagnostics, based on different emission-line ratios, are available, each with their own advantages and disadvantages. We chose to consider diagnostics that are calibrated using high-z galaxies or their low-redshift analogues, and that are least sensitive to the effects of ionization. These are the  $\hat{R}$  diagnostic from Laseter et al. (2024), and the  $R_{23}$  diagnostics from Nakajima et al. (2022) and Sanders et al. (2024). In addition to calibrating multiple diagnostics on their full galaxy sample, Nakajima et al. (2022) also provide H $\beta$  equivalent width (EW)-dependent calibrations for their low-metallicity sample  $(12 + \log(O/H) \sim 8.0)$ . However, we unfortunately do not detect the galaxy continuum in our NIRSpec data, and are therefore unable to measure  $H\beta$  EW. In this work, we therefore adopt the diagnostic calibrated using the full available sample. From the dust-corrected line fluxes, we calculate the diagnostic line ratios  $R_2 = \log([O II] \lambda \lambda 3726, 3729/H\beta), R_3 = \log([O III] \lambda 5007/H\beta),$  $R_{23} = \log(([O II] \lambda \lambda 3726, 3729 + [O III] \lambda \lambda 4959, 5007)/H\beta), \text{ and } \hat{R}$  $= 0.47 R_2 + 0.88 R_3$  from Laseter et al. (2024).

#### 4.3.1 Selecting the appropriate metallicity branch

A drawback of all three diagnostics used here is that they are double branched with a turnover that can yield two metallicity solutions for a given line ratio. However, for the  $R_{23}$  values we measure, the Sanders et al. (2024)  $R_{23}$  diagnostic has no valid upper branch solutions due

<sup>&</sup>lt;sup>2</sup>https://jwst-docs.stsci.edu/jwst-calibration-status/nirspec-calibration-status/nirspec-fixed-slit-calibration-status#gsc.tab=0

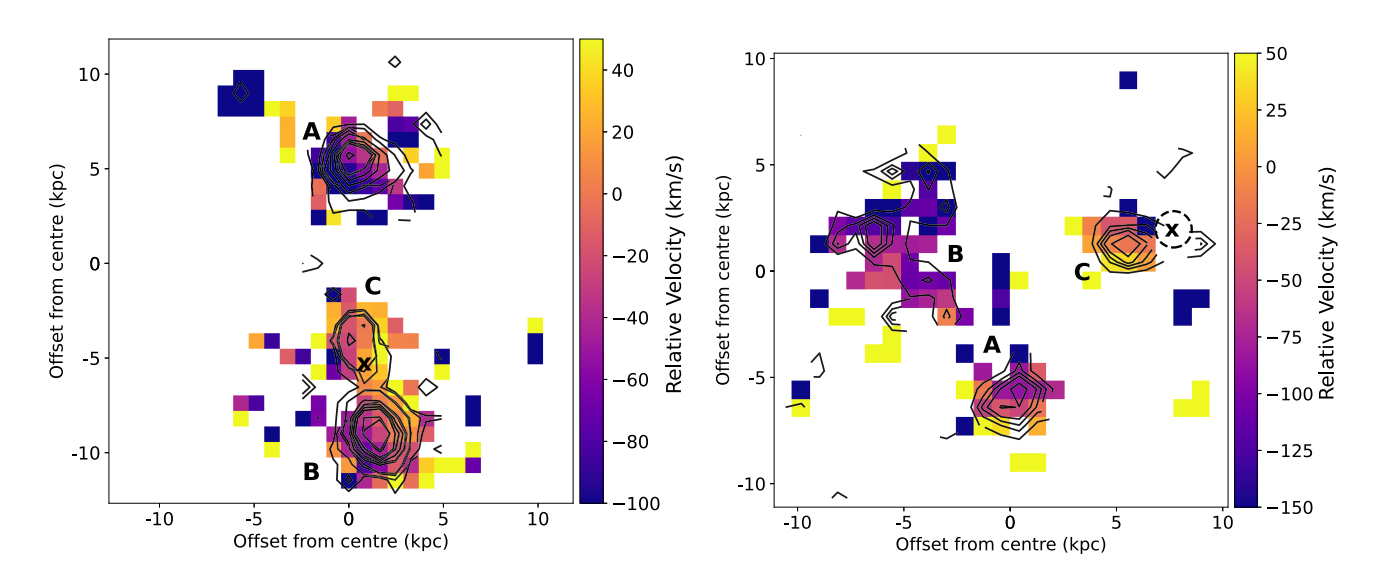


Figure 3. Maps showing the velocity offsets across the three detected star-forming components in GRB 050820A on the left-hand panel and in GRB 150403A on the right relative to the GRB hosting component (i.e. component C in both). The contours trace the flux strength of  $[O III] \lambda 5007$  line emission as in Figs 1 and 2. Bright spaxels represent regions that are redshifted relative to the GRB hosting component and dark spaxels show blueshifted regions.

to its shorter validity range of metallicities. Therefore, we exclude Sanders et al. (2024)  $R_{23}$  from the reported metallicity results. Nevertheless, we provide the lower branch solutions in Table B1.

The turnover for the Laseter et al. (2024)  $\hat{R}$  diagnostic is at  $12 + \log(O/H) = 8.12$ , while for the two  $R_{23}$  diagnostics, it is approximately 8.00. In order to determine whether to use the lower or upper branch solutions, we considered several additional factors for both galaxies. First, solutions calculated in this work were compared to the GRB afterglow absorption line metallicities. For GRB 050820A, Wiseman et al. (2017a) reported a sightline host galaxy metallicity [M/H] =  $-0.49 \pm 0.10$ , which corresponds to an oxygen abundance  $12 + \log(O/H) = 8.20 \pm 0.10$ . For GRB 150403A, the absorption metallicity was  $[M/H] = -0.92 \pm 0.05$ (Bolmer et al. 2019), corresponding to  $12 + \log(O/H) = 7.77 \pm$ 0.05. The absorption line metallicities along the GRB line of sight thus suggest an upper branch solution for GRB 050820A and a lower branch for GRB 150403A. However, it remains unclear whether we should expect the absorption line metallicity, which probes the galaxy neutral gas, to be the same as the ionized gas within star-forming regions that we probe here with nebular emission lines (Schady et al. 2024).

We therefore also considered additional strong line diagnostics to help break the degeneracies between the two-branch solutions. Following the same procedure as in Curti et al. (2020), we combined the  $R_{23}$ ,  $R_3$ , and O32 diagnostics from Nakajima et al. (2022) into a single estimate and determined the metallicity that minimized the difference between the observed and predicted diagnostic line ratio, taking into account the uncertainties in the line ratios. Using this technique, we measure a metallicity of  $8.28 \pm 0.12$  for GRB 150403A component C and  $8.10 \pm 0.10$  for GRB 050820A component C, suggesting that for both host galaxies the upper branch solution provides the greatest mutual consistency with all line diagnostics considered here. It is worth noting that the result from this analysis in the case of GRB 150403A is strongly influenced by the O32 diagnostic, as it has the smallest uncertainty due to not relying on the H $\beta$  line. The O32

$$^{3}[M/H] = \frac{\log N_{M}}{\log N_{H}} - \frac{\log N_{M_{\odot}}}{\log N_{H_{\odot}}}$$
 for some element  $M$ 

diagnostic is known to be highly sensitive to ionization parameters (e.g. Kewley & Dopita 2002), which adds additional systematic uncertainty to the metallicity measured in component C of GRB 150403A.

Finally, we also consider the galaxy metallicity expected from scaling relations given by other measured characteristic properties. In the case of GRB 050820A, we measure an SFR of 5.4  $\pm$  2.0  $M_{\odot}$  yr<sup>-1</sup> in component C, and use the stellar mass of  $\log(M_{\star}/\mathrm{M}_{\odot}) = 9.29$  for the same component measured in Chen et al. (2009). Using the mass metallicity relation (MZR) from Sanders et al. (2021), we would expect a component C metallicity of  $12 + \log(O/H) = 8.30 \pm 0.03$ . Similarly, when considering the SFR dependence on the MZR described by the fundamental metallicity relation (FMR), we would expect a comparable metallicity of  $12 + \log(O/H) = 8.37 \pm 0.05$ based on the high-z FMR from Sanders et al. (2021). The results obtained again support an upper branch solution for component C. Similar outcomes were obtained for the other components after performing the same analysis and therefore we report the upper branch solutions in Table 2. It is worth noting one caveat with this method, which is that Sanders et al. (2021) use the 'B18' (Bian, Kewley & Dopita 2018) metallicity diagnostic in their determinations of the MZR and FMR that is also based on strong-line calibrations.

For GRB 150403A component C, we only have a lower limit on the SFR due to our uncertain dust correction. We therefore refrain from making a similar analysis as in the case of GRB 050820A. We are, however, able to use the measured SFRs of components A and B, and, assuming they are main-sequence galaxies, combine these with the galaxy main sequence (SFR– $M_{\star}$  relation) from Sanders et al. (2021) to obtain a stellar mass estimate of  $\log(M_{\star}/\mathrm{M}_{\odot}) = 8.91 \pm 0.21$  and  $9.33 \pm 0.17$ , respectively. For these masses the Sanders et al. (2021), MZR predicts a metallicity  $12 + \log(\mathrm{O/H}) = 8.22 \pm 0.11$  for component A and  $8.33 \pm 0.09$  for component B. However, it is also worth noting that there is a large systematic uncertainty associated to these metallicity estimates given the large scatter in both the galaxy main sequence and the MZR.

Although the relations used within the methods above rely on various assumptions and empirical relations, all estimates consistently

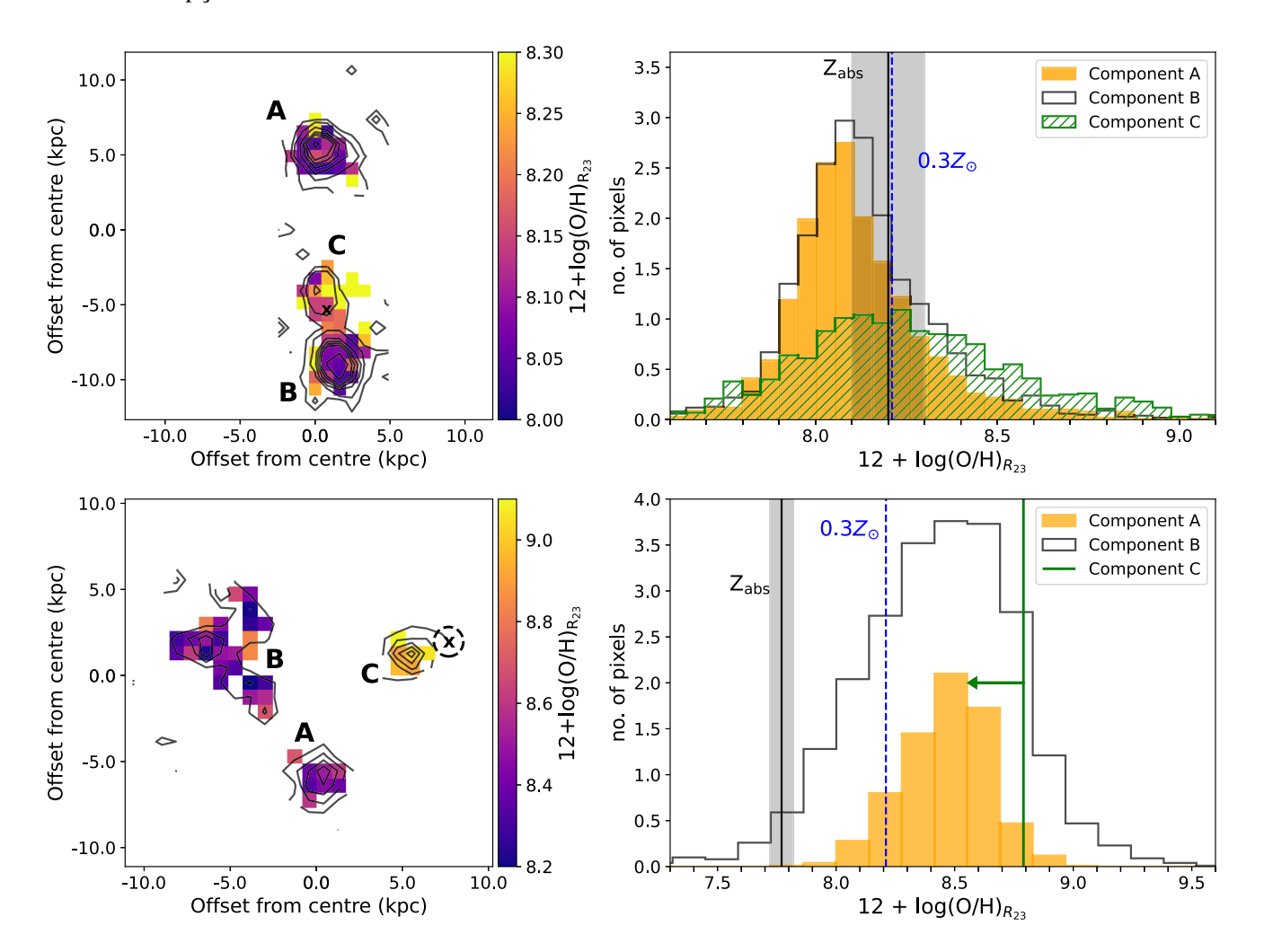


Figure 4. Metallicity variation across the two GRB host galaxies. The top row corresponds to GRB 050820A, and the bottom row to GRB 150403A. Left: gas-phase metallicity derived using the  $R_{23}$  diagnostic from Nakajima et al. (2022), with contours tracing [O III] λ5007 flux. For GRB 150403A component C, the metallicities are represented using  $1\sigma$  upper limits. Right: metallicity distributions of components A (filled orange), B (black outline), and C (hatched green), from the metallicity maps obtained by MC sampling from the metallicity maps. The solid, black vertical lines indicate the GRB afterglow absorption metallicity,  $Z_{abs}$ , converted to an equivalent oxygen abundance with its  $1\sigma$  uncertainty represented by the shaded region. Finally, the theoretical metallicity cap of  $0.3Z_{\odot}$  predicted by the single-star collapsar model is indicated by the dashed, vertical blue line. In the bottom-right panel, the upper limit metallicity on component C is represented by the vertical green line and the leftwards arrow.

indicate an upper branch solution with the exception of the absorption metallicity of GRB 150403A. We therefore adopt the upper branch solution for both host galaxies.

#### 4.3.2 Metallicity distribution

In addition to reporting the total integrated and component-based  $\hat{R}$  and  $R_{23}$  metallicities, and line ratios in Table 2, as was done in Schady et al. (2024), we also determine the metallicity at each IFU pixel to produce metallicity maps and study the metallicity variations across the two systems. In Fig. 4, we show the Nakajima et al. (2022)  $R_{23}$  metallicity maps in the left-hand panel for the host galaxies of GRB 050820A (top row) and GRB 150403A (bottom row). Similarly, in Fig. 5, we show the Laseter et al. (2024)  $\hat{R}$  metallicity maps for the two host galaxies. For the metallicity maps, the same masking criteria as in Fig. 3 is applied, removing all spaxels with [O III]  $\lambda$ 5007 SNR < 2. Additionally, in Figs 4 and 5, we also mask those spaxels for which our H $\beta$  fits failed. In addition to the

metallicity maps, we also show the metallicity distribution within each of the components in the right-hand panels of both figures. To take into account the measurement metallicity uncertainties on the generated histogram, we applied a Monte Carlo (MC) sampling, where we randomly selected the metallicity of each pixel from a Gaussian distribution centred at the measured pixel metallicity with a width corresponding to the metallicity  $1\sigma$  uncertainty. We ran this 100 times, producing a histogram after each run, and the average of these 100 realizations is then used to generate an MC-averaged histogram for each component. The filled orange, solid black, and hashed green histograms in the right-hand panels of Figs 4 and 5 correspond to the results from our MC analysis for components A, B, and C, respectively. Note that for GRB 150403A (bottom panels), a green vertical line with a leftwards arrow is used to represent the upper limit placed on the measured metallicity value instead of a histogram. On the same histograms, the GRB afterglow absorption metallicity is indicated with the labelled solid, black vertical line along with its  $1\sigma$  uncertainty in shaded regions. Finally,

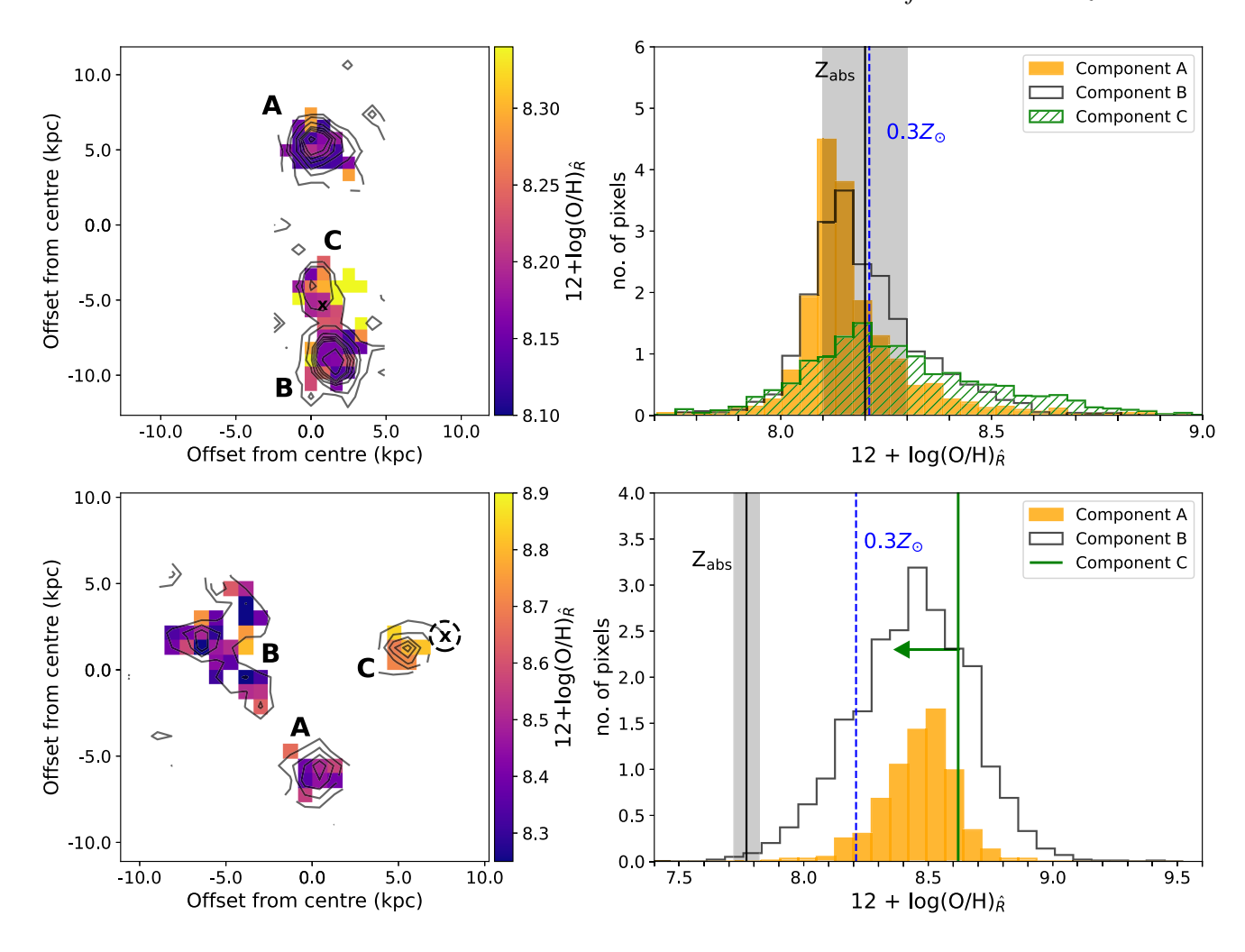


Figure 5. Figure showing the  $\hat{R}$  metallicity maps from Laseter et al. (2024) on the left, and the histograms representing the distribution of metallicities across the three components on the right for GRB 050820A (top row) and GRB 150403A (bottom row).

the  $0.3~Z_{\odot}$  metallicity cap predicted by the long GRB collapsar model is indicated with a blue, vertical dashed line.

The metallicity maps for GRB 050820A (Figs 4 and 5, top-left panels) show no obvious patterns of variation or gradients. However, components A and B exhibit a slightly inverted metallicity gradient, with lower metallicities in the centres and higher metallicities in the outskirts. In contrast, the histograms in the top panels of Figs 4 and 5 indicate that the metallicity distributions across the three components are largely consistent, apart from a few outlier spaxels.

For the likely host galaxy of GRB 050820A (component C), we measure metallicities of  $8.24 \pm 0.25$  and  $8.27 \pm 0.18$  using the Nakajima et al. (2022)  $R_{23}$  and Laseter et al. (2024)  $\hat{R}$  diagnostics, respectively. From the IFU data, we also determine the metallicity at the GRB location to be  $8.17 \pm 0.22$  and  $8.19 \pm 0.15$  for the Nakajima et al. (2022)  $R_{23}$  and Laseter et al. (2024)  $\hat{R}$  diagnostics, respectively. All four measurements are consistent with the absorption metallicity, which is equivalent to an oxygen abundance of  $12 + \log(O/H) = 8.20 \pm 0.10$  (Wiseman et al. 2017a). This can also be seen in the rightmost top panels of Figs 4 and 5, where the vertical line indicating the absorption metallicity,  $Z_{abs}$ , lies within the metallicity distribution of all three components. When compared to the maximum metallicity of long GRB progenitor stars predicted by the single-star collapsar model, the histograms of all three components peak at metallicities

below  $0.3\,Z_\odot$ , although it is noteworthy that component C, which we associate with the GRB, shows a broader distribution than components A and B. Nevertheless, the measured metallicity is consistent with being below  $0.3\,Z_\odot$  when considering uncertainties.

For GRB 150403A, the metallicity maps show no clear patterns. From the histograms on the bottom panels, all three components appear to be inconsistent ( $\sim$  0.6 dex higher) with the measured absorption metallicity of 7.77  $\pm$  0.05 for GRB 150403A (Bolmer et al. 2019). For component C, we only indicate the  $1\sigma$  upper limit on the measured metallicity due to the non-detection of the  $H\beta$  line for this component. The corresponding upper limits we measure are < 8.79 using the Nakajima et al. (2022)  $R_{23}$  diagnostic and < 8.62 using the Laseter et al. (2024)  $\hat{R}$  diagnostic.

We also note that, a new metallicity calibration was published by Scholte et al. (2025), providing a recalibration of the Laseter et al. (2024)  $\hat{R}$  diagnostic using a larger sample of high-redshift galaxies. We tested our results with the updated  $\hat{R}$  calibration and found them to be consistent with the Laseter et al. (2024)  $\hat{R}$  values reported in Table 2, within  $1\sigma$ .

#### 4.4 The ISM properties

The Baldwin, Phillips & Terlevich (BPT) diagram of  $\log([O III]\lambda 5007/H\beta)$  against  $\log([N II]\lambda 6584/H\alpha)$  is effective at

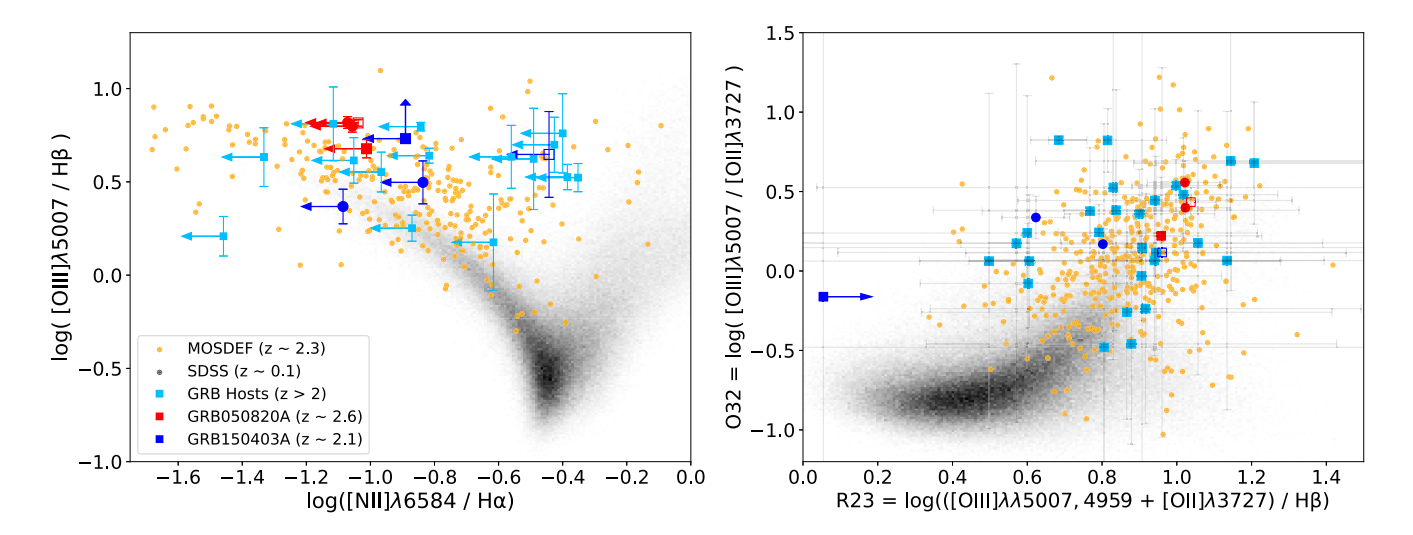


Figure 6. Left: the N2-BPT diagram with  $1\sigma$  upper limits on [N II]/Hα. Right: the O32 versus R23 diagram. In both diagrams, the star-forming components presented in this work are plotted in red (for GRB 050820A) and blue (GRB 150403A) with the likely host galaxies (component C) represented with filled squares and the galaxy-integrated measurements with empty squares. Finally, the remaining two star-forming components from both observations (components A and B) are represented as blue and red circles. Note that for GRB 150403A component C, additional  $1\sigma$  lower limits are placed on line ratios containing Hβ. The cyan data points represent a sample of high-redshift (z > 2) GRB hosts observed with X-shooter (Krühler et al. 2015), and with JWST/NIRSpec in fixed slit mode (Schady et al. 2024), including the host galaxy of GRB 050505 at z = 4.27 (Inkenhaag et al., in preparation). Orange data points are high-redshift ( $z \sim 2.3$ ) star-forming galaxies from the MOSDEF survey, while the black data points represent local star-forming galaxies from the SDSS catalogue.

identifying the dominant ionization mechanism responsible for the observed emission line, and it highlights differences in the ionization properties of local and distant galaxies (Baldwin, Phillips & Terlevich 1981). The  $O32 = \log([O III] \lambda 5007/[O II] \lambda \lambda 3726, 3729))$  versus  $R_{23}$  diagram similarly depicts the ISM conditions of the nebular gas (e.g. Nakajima & Ouchi 2014; Paalvast et al. 2018; Runco et al. 2021), with R23 tracing metallicity and O32 tracing ionization. The BPT diagram and the O32 versus R23 diagrams in Fig. 6 show the emission-line properties for each of the three components identified in our two likely host galaxies as filed squares as well as the total integrated estimates as empty squares. The remaining two starforming components are represented with circles. For comparison, we also show a sample of 15 high-redshift (z > 2) GRB host galaxies on both diagrams as the cyan data points from Krühler et al. (2015) and Schady et al. (2024) as well as GRB 050505 observed with JWST at  $z \sim 4.3$  (Inkenhaag et al., in preparation). For the majority of GRB host galaxies [N II] λ6584 is undetected, and we thus use the  $1\sigma$  upper limit, which is indicated by the leftward arrows. For GRB 150403A component C, additional  $1\sigma$ lower limits are shown for the  $\log([O III]\lambda 5007/H\beta)$  and R23 line ratios due to the non-detection of H $\beta$ . Grey data points represent the local star-forming galaxies from the seventh data release of the Sloan Digital Sky Survey (SDSS) (Abazajian et al. 2009), while orange data points represent high-redshift ( $z \sim 2.3$ ) star-forming galaxies from MOSFIRE Deep Evolution Field (MOSDEF) survey (Kriek et al. 2015; Reddy et al. 2015). Only SDSS and MOSDEF galaxies with  $H\beta$ , [O II]  $\lambda\lambda$ 3726, 3729, and [O III]  $\lambda$ 5007 fluxes with SNR > 3 are plotted.

High-redshift star-forming galaxies are expected to shift upwards on the BPT diagram compared to local galaxies due to the harder ionization fields and higher ionization parameters at higher redshift (Kewley et al. 2013; Shirazi, Brinchmann & Rahmati 2014; Steidel et al. 2014). This behaviour is observed in the MOSDEF galaxy at  $z\sim 2.3$  (orange) and the z>2 GRB host galaxy sample from Krühler et al. (2015) and Schady et al. (2024, cyan), which lie

systematically above the SDSS galaxies (Fig. 6, left-hand panel). For GRB 050820A, all three components, as well as the total integrated data point, appear relatively consistent with one another. For GRB 150403A, components A and B appear consistent with the distribution of high-redshift GRB hosts and galaxies. In the case of component C, we only have limits on the line ratios due to the non-detection of [NII]  $\lambda 6584$  and H $\beta$ . Nevertheless, the starforming components studied in this work lie in a region of the BPT diagram consistent with other GRB host and star-forming galaxies at z > 2. In the right-hand panel of Fig. 6, we show the O32 versus R23 line ratios for the same sample of galaxies as plotted in the BPT diagram. We again see an offset in the z > 2galaxies relative to the SDSS sample, with high-redshift galaxies clustering around the tail end of the distribution of local SDSS galaxies, corresponding to the generally higher ionization fields and lower abundances in high-redshift galaxies as already seen in the BPT diagram (e.g, Shapley et al. 2015). In this parameter space our sample of star-forming components again lie within the same region of the parameter space as occupied by other high-redshift GRB hosts and star-forming galaxies. This indicates that these GRB host galaxies are not particularly unusual or distinct compared to high-z star-forming galaxies.

#### 5 DISCUSSION

#### 5.1 Relation between components

In the host galaxy observations of both GRB 050820A and GRB 150403A three spatially distinct emission components are clearly visible. Aside from their projected separation, the IFU data provide key emission-line properties (Section 4) which we use to determine the relation between the detected components and to the GRB itself. We have labelled these components A, B, and C, and in both cases the GRB position is spatially located closest to component C.

#### 5.1.1 GRB 050820A

Within the galaxy complex of GRB 050820A, component A is well separated from the other two components, with a projected physical separation of  $\sim 8$  kpc (Fig. 1; see also Chen et al. 2009). This separation is  $\sim$  4 times larger than the average size of starforming galaxies at similar redshifts (Ribeiro et al. 2016), suggesting that component A is a separate galaxy to the GRB host, as already concluded in Chen et al. (2009). On the other hand, components B and C exhibit a smaller velocity offset ( $-26 \pm 8 \text{ km s}^{-1}$ ), and their separation of less than 3 kpc is more consistent with them being part of a single galaxy. Additionally, emission is observed across components B and C in continuum as detected in the HST broad-band imaging, as well as in our  $[O III] \lambda 5007$  surface brightness maps (see Fig. 1). However, interpreting them as a single system would imply a total diameter of  $\sim 8$  kpc, which, as stated above, would be far larger than the average size of star-forming galaxies at a similar redshift. Furthermore, the morphology and dynamics of the system do not appear disc-like (see Fig. 1), making it more likely that components B and C are also separate galaxies.

We can use the velocity offsets measured between the three components, combined with the GRB afterglow absorption spectra from Prochaska et al. (2007) to build a 3D picture of the system. The absorption spectra reveal broad absorption features spanning up to  $\Delta v \sim 400 \; \mathrm{km s^{-1}}$ , but due to degeneracies between local velocities and cosmological redshift, we are unable to robustly identify the origin of the high velocity absorbing material. As described in Chen (2012), either component C lies in front of components A and B and is falling towards them, or it is located behind A and B but moving away from component B. In our NIRSpec IFS data, we additionally measure a velocity offset of  $-97 \pm 17 \text{ kms}^{-1}$  for component C relative to the GRB absorption redshift of 2.61469 (Prochaska et al. 2007). Given the projected proximity between the GRB and component C, it is natural to assume that component C is the host galaxy, and the afterglow spectrum shows blueshifted absorption features consistent with the velocity offset measured to component C. This would therefore imply that turbulence within the host galaxy (i.e. component C) contributes to the velocity spread of  $\sim 100 \; \mathrm{km} \, \mathrm{s}^{-1}$  observed in the afterglow spectrum, with additional absorption at larger velocities originating from material within B and in tidal debris between components A and B, as suggested in Chen (2012).

An additional reason to favour a scenario in which component C is the GRB host galaxy and lies behind components A and B is the detection of the excited line Si II\*λ1264 absorption feature in the GRB absorption spectrum consistent with the velocity of component B. Si II\*λ1264 is an excited-state transition and previous time evolution observations of excited lines in GRB afterglow spectra have indicated that the GRB is the source of excitation, placing the absorbing material within a few kpc of the GRB (Vreeswijk et al. 2007; D'Elia et al. 2010; Vreeswijk et al. 2013; Saccardi et al. 2023). This is consistent with the measured separation between components B and C, which may help break the degeneracy between the two possible scenarios, ultimately favouring the interpretation that the GRB host lies behind the other two interacting galaxies.

#### 5.1.2 GRB 150403A

Our IFU observations of the host galaxy of GRB 150403A reveal a significant projected separation ( $\sim$  7 kpc) between the component

likely to have hosted the GRB (component C) and the other two components (see Fig. 2). This separation suggests that component C is a distinct galaxy that is interacting with components A and B, which are offset from C by  $-68 \pm 15$  and  $-96 \pm 15$  km s<sup>-1</sup>, respectively. The smaller velocity offset between A and B ( $\sim 28$  km s<sup>-1</sup>), combined with a smaller projected separation (< 3 kpc), may imply that they are two bright emission regions of a single galaxy. However, if components A and B were a single galaxy, the combined projected diameter would then be  $\sim 11$  kpc, which, as was the case for GRB 050820A, is far larger than what is typically observed at z > 2. Also, given the morphology and dynamics indicated in Fig. 3, it seems more likely that the three components identified in the data cube correspond to three closely interacting galaxies.

Similar to GRB 050820A, components A and B, which are unlikely to have hosted the GRB, are blueshifted from the likely host galaxy (component C). To construct a 3D picture of the galaxy system, we again compare the kinematics measured from our IFU data to those derived from the GRB afterglow spectrum presented in Bolmer et al. (2019). Absorption features are detected in the absorption spectrum at -60 and -100 km s<sup>-1</sup> from the GRB in several lines (e.g. O<sub>I</sub>, Mn II, and Mg II), consistent with the velocity offsets that we measure between the likely GRB host galaxy and components A and B, respectively. This would imply that components A and B lie in front of the host galaxy (component C), and thus as was the case for GRB 050820A, the host galaxy of GRB 150403A appears to be moving away from the other two companion galaxies. Absorption features at higher velocities at -150 and -200 km s<sup>-1</sup> are also observed relative to component C. However, these are undetected in emission and thus correspond to diffuse gas that may originate from galaxy inflows/outflows, possibly related to interactions between components A and B.

#### 5.1.3 Examples of interacting GRB host galaxies

There are examples of other GRB hosts that show evidence of interaction with another galaxy from their morphologies or kinematics, such as GRB 980425 (Arabsalmani et al. 2015, 2019), GRB 980613 (Djorgovski, Bloom & Kulkarni 2003), GRB 990123 (Bloom et al. 1999; Fruchter et al. 1999), GRB 080810 (Wiseman et al. 2017b), GRB 100219A (Thöne et al. 2013), and GRB 171205A (Arabsalmani et al. 2022). Similar to the host galaxies studied in this paper, GRB 980425, GRB 980613, GRB 990123, and GRB 080810 were also found in host galaxies that are surrounded by multiple neighbouring components. Additionally, afterglow absorption spectrum of GRB 090323 and GRB 080810 showed absorption features at large velocity offsets indicative of a companion galaxy (Savaglio et al. 2012; Wiseman et al. 2017b).

The hosts of GRB 050820A and GRB 150403A show evidence of interactions, both through the morphologies of their observed systems and through the absorbing features seen in the GRB afterglow spectra. Merging or interacting galaxies can trigger star formation (Somerville et al. 2001; Teyssier et al. 2010), and it may therefore be reasonable to expect an increase in long GRBs occurring within interacting galaxy systems. Furthermore, given the increasing merger rate with redshift up to  $z \sim 2$  (Le Fèvre et al. 2000), it is likely that more interacting galaxies will be observed as GRB hosts in the high-redshift ( $z \sim 2-3$ ) Universe. Quantifying the importance of galaxy interactions in the formation of long GRBs will require a complete study on the morphological and kinematic properties

of GRB host galaxies relative to the general star-forming galaxy population.

#### 5.2 Implications for the $0.3Z_{\odot}$ theoretical threshold

The collapsar model predicts a  $0.3Z_{\odot}$  metallicity threshold for progenitors of long GRBs (Woosley 1993). Consequently, a similar cut-off is expected in the star-forming regions hosting a GRB event. For GRB 050820A, both the emission and absorption metallicity measurements lie close to  $0.3Z_{\odot}$  ( $\sim 8.21$ ). However, the majority of the spaxels fall below this value (see top-right panel in Fig. 4), and for component C, the measured metallicity is consistent with being below  $0.3Z_{\odot}$  when considering uncertainties. This therefore suggests that our results for GRB 050820A are not in strong tension with the standard collapsar model.

For GRB 150403A, the metallicity of component C is not well constrained and we therefore report this as an upper limit. The remaining two components appear to have metallicities above the collapsar model theoretical threshold (see the bottom histograms in Figs 4 and 5), although consistent within the uncertainties (see Table 2). They are, however, significantly larger than the absorption line metallicity, which may imply that these two components are more metal-rich than component C.

Although the metallicities of both GRB hosts lie close to or above the  $0.3Z_{\odot}$  threshold, several previous observations of GRB hosts, both nearby (z < 1) and more distant (z > 2), have reported metallicities comparable to or higher than  $0.3Z_{\odot}$  (e.g. Krühler et al. 2015). The discrepancies between emission and absorption line metallicities introduce significant uncertainty regarding whether the emission-line metallicities truly trace the metallicity of the progenitor environment. Considering these factors, along with the uncertainties in high-redshift metallicity diagnostics, we do not consider the metallicities measured in this paper to be significantly unusual.

#### 5.3 The characteristic host galaxy properties

The flux estimates trace the SFR as the emission is most likely due to ionization by young stars. For the observations of GRB 050820A, the component within which the GRB is located is the faintest region among all three components. However, this does not necessarily indicate that the GRB happened in a low star-forming region consistent with many previous observations (e.g. Bloom, Kulkarni & Djorgovski 2002; Fruchter et al. 2006; Krühler et al. 2015, 2017). The estimates done using the H $\alpha$  flux yield an SFR of  $5.4 \pm 2.0~M_{\odot}\,\text{yr}^{-1}$  for the component associated with the GRB location. Other hosts have been observed in the past for which the observed location of the GRB was found not to lie within the region with the highest SFR (e.g. Krühler et al. 2011; Izzo et al. 2017). Nevertheless, component C is still a region with significant star formation. Compared to the larger population of long GRB hosts studied by Krühler et al. (2015), the SFR of component C appears lower than the median value of  $\sim 20~M_{\odot}\,\text{yr}^{-1}$  observed for long GRB hosts at z > 2. This lower SFR could be attributed to the host galaxy of GRB 050820A being a tidal dwarf galaxy, as suggested by Chen (2012), since typical long GRB hosts generally exhibit higher SFRs than tidal dwarf galaxies (Ploeckinger et al. 2015; Lee-Waddell et al. 2016). Alternatively, the host galaxy may still be in the process of transitioning to a higher SFR due to the ongoing interactions with neighbouring galaxies, similar to the starburst phase transitions observed in particularly massive GRB hosts by Nadolny et al. (2023).

Component C also has a mass estimate of  $\log(M_{\star}/M_{\odot}) \sim 9.3$  from the literature (Chen et al. 2009). Using this estimate and the work

done by Thorne et al. (2021) from the Deep Extragalactic Visible Legacy Survey (DEVILS), it is possible to check where this host lies on the galaxy main sequence. We see that the SFR estimated in this work lies slightly below the point where the number density of galaxies peaks in galaxy main-sequence plots at the redshift bins of both 2.2 < z < 2.6 and 2.6 < z < 3.25 (see fig. 13 in Thorne et al. 2021). Similarly, comparing with  $z \sim 2.3$  galaxies from the MOSDEF survey with a mass range  $\log(M_{\star}/\rm M_{\odot}) = 9.15-9.68$  also reveals that component C has a lower SFR than the measured median value of  $11.6~\rm M_{\odot}~\rm yr^{-1}$  (Sanders et al. 2015).

On the other hand, had the galaxy complex not been imaged with HST beforehand, revealing multiple extended components, the JWST follow-up may well have been planned in slit-based rather than IFU mode. In such a scenario, component B might have been incorrectly assigned as the host galaxy instead of component C, and the resulting SFR would be consistent with both the MOSDEF and the DEVILS samples as well as other long GRB hosts within Krühler et al. (2015). Even with the HST observation, a fixed slit observation of the host galaxy could have included contamination from component B, leading to an overestimation of the measured SFR. This may already be the case for some high redshift (z > 2) GRB host studies that lack spatially resolved observations. If the SFR in these hosts is overestimated due to contamination, it would mean that the SFR of component C is closer to being consistent with other high-redshift (z > 2) GRB hosts.

Observations of GRB 150403A show that component C, with which the GRB is affiliated, shows significant line emission and an SFR which is  $39^{+76}_{-36}~M_{\odot}~yr^{-1}$ . The SFR is largely unconstrained due to the uncertainty on host galaxy dust corrections. However, the uncertainty at the lower end is set by the fact that the SFR cannot be lower than the dust uncorrected H $\alpha$  flux, corresponding to an SFR  $\sim 3~M_{\odot}~yr^{-1}$ . This shows that GRB 150403A is also affiliated with a star-forming region, consistent with GRB 050820A and previous long GRB host galaxy observations (e.g. Gorosabel et al. 2005; Sollerman et al. 2005; Krühler et al. 2011). Currently, no mass estimates are present in the literature for the host of GRB 150403A, by lack of sensitive long-wavelength photometric measurements of the host.

As was the case for GRB 050820A, if the afterglow of GRB 150403A had not been well localized, it would be unclear which of the three galaxies was the host. Given the separation of component C from the other two components, contamination from neighbouring regions is not expected. However, misidentifying the host galaxy would have been a possibility.

#### 6 CONCLUSIONS

We present our spectroscopic analysis of the intermediate redshift host galaxies of GRB 050820A and GRB 150403A observed with JWST/NIRSpec using IFU data. These IFU observations are among the first observations where we were able to resolve multiple star-forming components at the GRB location within redshift z>2 galaxies instead of single-slit observations. This provided the opportunity of comparing the ISM properties and characteristics such as metallicities of these resolved regions with single-slit observations of high-redshift GRB hosts from earlier works. In addition, we also compared the line diagnostic properties of our sample with larger samples characterizing the broader star-forming populations in the local Universe and at  $z\sim 2.3$ . Having IFU observations further allowed for the kinematics of the observed systems to be studied making it possible to build a 3D picture of the interacting galaxies.

Based on our analysis of the velocity offsets and the spatial separation between the multiple star-forming components in each observation, we believe that the observed targets are interacting with one another and that it is likely that all components are independent galaxies. The exception to this could be the host of GRB 050820A which appears to be a tidal dwarf galaxy that formed during the interactions of the other two galaxies, which is also suggested in Chen (2012). Comparisons between the spatial and velocity offsets of the galaxies measured in our IFU data combined with the GRB afterglow absorption kinematics suggest that, in both cases, the neighbouring galaxies may lie between us and the host galaxies. Additionally, both GRB hosts appear to be moving away from their neighbouring galaxies.

Both GRB hosts were observed to be found in star-forming galaxies in line with expectations and previous observations (Le Floc'h et al. 2003; Fruchter et al. 2006; Perley et al. 2016). Furthermore, the ISM properties of the GRB host galaxies are consistent with other GRB host galaxies and star-forming galaxies found at z > 2.

For GRB 050820A, we find that both the metallicity at the GRB location and the metallicity of the overall host galaxy is consistent with the absorption metallicity of  $8.20\pm0.10$  (Wiseman et al. 2017a). For GRB 150403A, we report the metallicity of the host galaxy as upper limits due to non-detection of H $\beta$ . However, we note that the neighbouring galaxies (components A and B) appear to have metallicities that are  $\sim0.6$  dex higher than the absorption metallicity of 7.77  $\pm$  0.05 (Bolmer et al. 2019), which may imply that they are more-metal rich than the GRB host galaxy (i.e. component C).

In some of our measurements of the SFRs and certain line diagnostics, we observed differences between the values obtained for individual components and those averaged across all components. This shows the importance of spatially resolved spectroscopy, particularly for high-redshift objects. IFU observations allow to create maps of parameters such as metallicity, SFRs, and line ratios, revealing spatial variations across a galaxy. Furthermore, the kinematic information content provides insights into dynamical characteristics, such as rotational patterns, velocity dispersions, and evidence of interactions or mergers. This information can improve our understanding of high-redshift GRB host galaxies and of the broader galaxy population traced by long GRBs. As observational campaigns continue to expand with instruments like JWST, we may find more GRB host galaxies near star-forming companions like those observed in this study. This could provide further evidence supporting the hypothesis that GRB hosts are often irregular galaxies (Conselice et al. 2005; Fruchter et al. 2006; Wainwright et al. 2007), possibly shaped by past interactions with neighbouring galaxies. Therefore, it is essential to conduct such spectroscopic analyses with larger samples, which would also allow us to obtain more robust conclusions about how high-redshift GRB hosts differ from their local counterparts or how they differ from broader galaxy populations at similar redshifts.

#### **ACKNOWLEDGEMENTS**

PS acknowledges support from the UK Science and Technology Facilities Council, grant reference ST/X001067/1. AR acknowledges support by PRIN-MIUR 2017 (grant 20179ZF5KS). RLCS is supported by the Leverhulme Trust, grant RPG-2023-240. LC is supported by DFF/Independent Research Fund Denmark, grant-ID 2032–00071. The Cosmic Dawn Center is funded by the Danish National Research Foundation under grant DNRF140. This work makes use of the PYTHON packages NUMPY (v.1.26.4; Harris et al. 2020), MATPLOTLIB (v.3.8.0; Hunter 2007), UNCERTAINTIES

(v.3.1.7; http://pythonhosted.org/uncertainties), SPECUTILS (v.1.13.0; Earl et al. 2024), PANDAS (v.2.2.1; The pandas development team 2020) and ASTROPY (v.5.3.4; Astropy Collaboration 2013, 2018, 2022)

#### DATA AVAILABILITY

The data underlying this article are available in the MAST Data Discovery Portal at https://stdatu.stsci.edu/datadownloads.html, and can be accessed with proposal ID 2344.

#### REFERENCES

```
Abazajian K. N. et al., 2009, ApJS, 182, 543
Abbott B. P. et al., 2017, ApJ, 848, L13
Arabsalmani M. et al., 2019, MNRAS, 485, 5411
Arabsalmani M., Roychowdhury S., Renaud F., Burkert A., Emsellem E., Le
   Floc'h E., Pian E., 2022, AJ, 164, 69
Arabsalmani M., Roychowdhury S., Zwaan M. A., Kanekar N., Michałowski
   M. J., 2015, MNRAS, 454, L51
Astropy Collaboration, 2013, A&A, 558, A33
Astropy Collaboration, 2018, AJ, 156, 123
Astropy Collaboration, 2022, ApJ, 935, 167
Bacon R. et al., 2010, in McLean I. S., eds, Ramsay S. K., Takami H. Ground-
   based and Airborne Instrumentation for Astronomy III. Vol. 7735, Society
   of Photo-Optical Instrumentation Engineers (SPIE) Conf. Ser., SPIE,
   Bellingham, p. 773508
Baldwin J. A., Phillips M. M., Terlevich R., 1981, PASP, 93, 5
Berger E. et al., 2005, Nature, 438, 988
Berger E., Cowie L., Kulkarni S., Frail D., Aussel H., Barger A., 2003, ApJ,
Bian F., Kewley L. J., Dopita M. A., 2018, ApJ, 859, 175
Blanchard P. K., Berger E., Fong W.-f., 2016, ApJ, 817, 144
Bloom J. et al., 1999, ApJ, 518, L1
Bloom J. S., Kulkarni S. R., Djorgovski S. G., 2002, AJ, 123, 1111
Böker T. et al., 2022, A&A, 661, A82
Bolmer J. et al., 2019, A&A, 623, A43
Cardelli J. A., Clayton G. C., Mathis J. S., 1989, ApJ, 345, 245
Chabrier G., 2003, PASP, 115, 763
Chen H.-W. et al., 2009, ApJ, 691, 152
Chen H.-W., 2012, MNRAS, 419, 3039
Christensen L., Hjorth J., Gorosabel J., 2004, A&A, 425, 913
Christensen L., Vreeswijk P., Sollerman J., Thöne C., Le Floc'h E., Wiersema
   K., 2008, A&A, 490, 45
Conselice C. J. et al., 2005, ApJ, 633, 29
Curti M., Mannucci F., Cresci G., Maiolino R., 2020, MNRAS, 491, 944
D'Elia V. et al., 2010, A&A, 523, A36
Djorgovski S., Bloom J., Kulkarni S., 2003, ApJ, 591, L13
           et al., 2024,
                                 astropy/specutils:
                                                                  Zenodo,
   doi:10.5281/zenodo.10681408
Eichler D., Livio M., Piran T., Schramm D. N., 1989, Nature, 340, 126
Ferrero P. et al., 2009, A&A, 497, 729
Ferruit P. et al., 2022, A&A, 661, A81
Fruchter A. et al., 2006, Nature, 441, 463
Fruchter A. S. et al., 1999, ApJ, 519, L13
Gorosabel J. et al., 2005, A&A, 444, 711
Graham J. F., Fruchter A. S., 2017, ApJ, 834, 170
Graham J., Fruchter A., 2013, ApJ, 774, 119
Greiner J. et al., 2008, PASP, 120, 405
Greiner J. et al., 2009, ApJ, 693, 1610
Harris C. R. et al., 2020, Nature, 585, 357
Hunter J. D., 2007, Comput. Sci. Eng., 9, 90
Izzo L. et al., 2017, MNRAS, 472, 4480
```

Jakobsen P. et al., 2022, A&A, 661, A80

Kennicutt R. C., Jr, 1998, ARA&A, 36, 189

Kelly P. L., Kirshner R. P., Pahre M., 2008, ApJ, 687, 1201

1856 B. Topçu et al. Kewley L. J., Dopita M. A., 2002, ApJS, 142, 35 Kewley L. J., Dopita M. A., Leitherer C., Davé R., Yuan T., Allen M., Groves B., Sutherland R., 2013, ApJ, 774, 100 Kistler M. D., Yüksel H., Beacom J. F., Hopkins A. M., Wyithe J. S. B., 2009, ApJ, 705, L104 Klebesadel R. W., Strong I. B., Olson R. A., 1973, ApJ, 182, L85 Klose S. et al., 2004, AJ, 128, 1942 Kriek M. et al., 2015, ApJS, 218, 15 Krühler T. et al., 2011, A&A, 534, A108 Krühler T. et al., 2015, A&A, 581, A125 Krühler T., Kuncarayakti H., Schady P., Anderson J. P., Galbany L., Gensior J., 2017, A&A, 602, A85 Laseter I. H. et al., 2024, A&A, 681, A70 Le Fèvre O. et al., 2000, MNRAS, 311, 565 Le Floc'h E. et al., 2003, A&A, 400, 499 Ledoux C., Vreeswijk P., Smette A., Fox A., Petitjean P., Ellison S., Fynbo J., Savaglio S., 2009, A&A, 506, 661 Lee-Waddell K. et al., 2016, MNRAS, 460, 2945 LeFevre O. et al., 2003, in Iye M., Moorwood F. M., eds, Instrument Design and Performance for Optical/Infrared Ground-based Telescopes. Proc. SPIE Conf. Ser. Vol. 4841, SPIE, Bellingham, p. 1670 Levan A. J. et al., 2023, Nat. Astron., 7, 976 Levan A. J. et al., 2024, Nature, 626, 737 Levesque E. M., Berger E., Kewley L. J., Bagley M. M., 2010a, AJ, 139, 694 Levesque E. M., Kewley L. J., Berger E., Zahid H. J., 2010b, AJ, 140, 1557 Li W., Chornock R., Leaman J., Filippenko A. V., Poznanski D., Wang X., Ganeshalingam M., Mannucci F., 2011, MNRAS, 412, 1473 López-Sánchez A. R., Esteban C., 2009, A&A, 508, 615 Nadolny J. et al., 2023, ApJ, 952, 125 Nakajima K. et al., 2022, ApJS, 262, 3 Nakajima K., Ouchi M., 2014, MNRAS, 442, 900 Narayan R., Paczyński B., Piran T., 1992, ApJ, 395, L83 Osterbrock D. E., 1989, Ann. New York Acad. Sci., 571, 99 Paalvast M. et al., 2018, A&A, 618, A40

Page K. L. et al., 2009, MNRAS, 400, 134 Pei Y. C., 1992, ApJ, 395, 130 Perley D. et al., 2016, ApJ, 817, 8 Planck Collaboration XIII, 2016, A&A, 594, A13

Ploeckinger S., Recchi S., Hensler G., Kroupa P., 2015, MNRAS, 447, Prochaska J. et al., 2007, ApJS, 168, 231

Rastinejad J. C. et al., 2022, Nature, 612, 223 Reddy N. A. et al., 2015, ApJ, 806, 259 Ribeiro B. et al., 2016, A&A, 593, A22 Rossi A. et al., 2012, A&A, 545, A77 Rossi A. et al., 2014, A&A, 572, A47 Runco J. N. et al., 2021, MNRAS, 502, 2600

Saccardi A. et al., 2023, A&A, 671, A84 Salvaterra R. et al., 2009, Nature, 461, 1258 Sanders R. L. et al., 2015, ApJ, 799, 138 Sanders R. L. et al., 2021, ApJ, 914, 19 Sanders R. L., Shapley A. E., Topping M. W., Reddy N. A., Brammer G. B., 2024, ApJ, 962, 24 Savaglio S. et al., 2002, GCN Circ., 1633, 1 Savaglio S. et al., 2012, MNRAS, 420, 627 Savaglio S., Glazebrook K., Le Borgne D., 2009, ApJ, 691, 182 Schady P. et al., 2024, MNRAS, 529, 2807 Schlafly E. F., Finkbeiner D. P., 2011, ApJ, 737, 103 Scholte D. et al., 2025, MNRAS Selsing J. et al., 2019, A&A, 623, A92 Shapley A. E. et al., 2015, ApJ, 801, 88 Shirazi M., Brinchmann J., Rahmati A., 2014, ApJ, 787, 120 Sollerman J., Östlin G., Fynbo J., Hjorth J., Fruchter A., Pedersen K., 2005, New Astron., 11, 103 Somerville R. S., Primack J. R., Faber S., 2001, MNRAS, 320, 504 Steidel C. C. et al., 2014, ApJ, 795, 165 Svensson K. M., Levan A., Tanvir N., Fruchter A., Strolger L.-G., 2010, MNRAS, 405, 57 Tanga M., Krühler T., Schady P., Klose S., Graham J. F., Greiner J., Kann D. A., Nardini M., 2018, A&A, 615, A136 Tanvir N. R. et al., 2004, MNRAS, 352, 1073 Tanvir N. R. et al., 2009, Nature, 461, 1254 Teyssier R., Chapon D., Bournaud F., 2010, ApJ, 720, L149 The pandas development team, 2020, pandas-dev/pandas: Pandas. Zenodo, doi:10.5281/zenodo.3509134 Thöne C. C. et al., 2024, A&A, 690, A66 Thöne C. et al., 2013, MNRAS, 428, 3590 Thorne J. E. et al., 2021, MNRAS, 505, 540 Troja E. et al., 2022, Nature, 612, 228 Vreeswijk P. et al., 2013, A&A, 549, A22 Vreeswijk P. M. et al., 2007, A&A, 468, 83 Wainwright C., Berger E., Penprase B. E., 2007, ApJ, 657, 367 Wiseman P., Perley D., Schady P., Prochaska J. X., de Ugarte Postigo A., Krühler T., Yates R., Greiner J., 2017b, A&A, 607, A107 Wiseman P., Schady P., Bolmer J., Krühler T., Yates R., Greiner J., Fynbo J., 2017a, A&A, 599, A24 Woosley S. E., 1993, ApJ, 405, 273 Woosley S., Bloom J., 2006, ARA&A, 44, 507 Yang Y.-H. et al., 2024, Nature, 626, 742 Zhang B., Pe'er A., 2009, ApJ, 700, L65

#### APPENDIX A: GAUSSIAN FITS TO STACKED **SPECTRA**

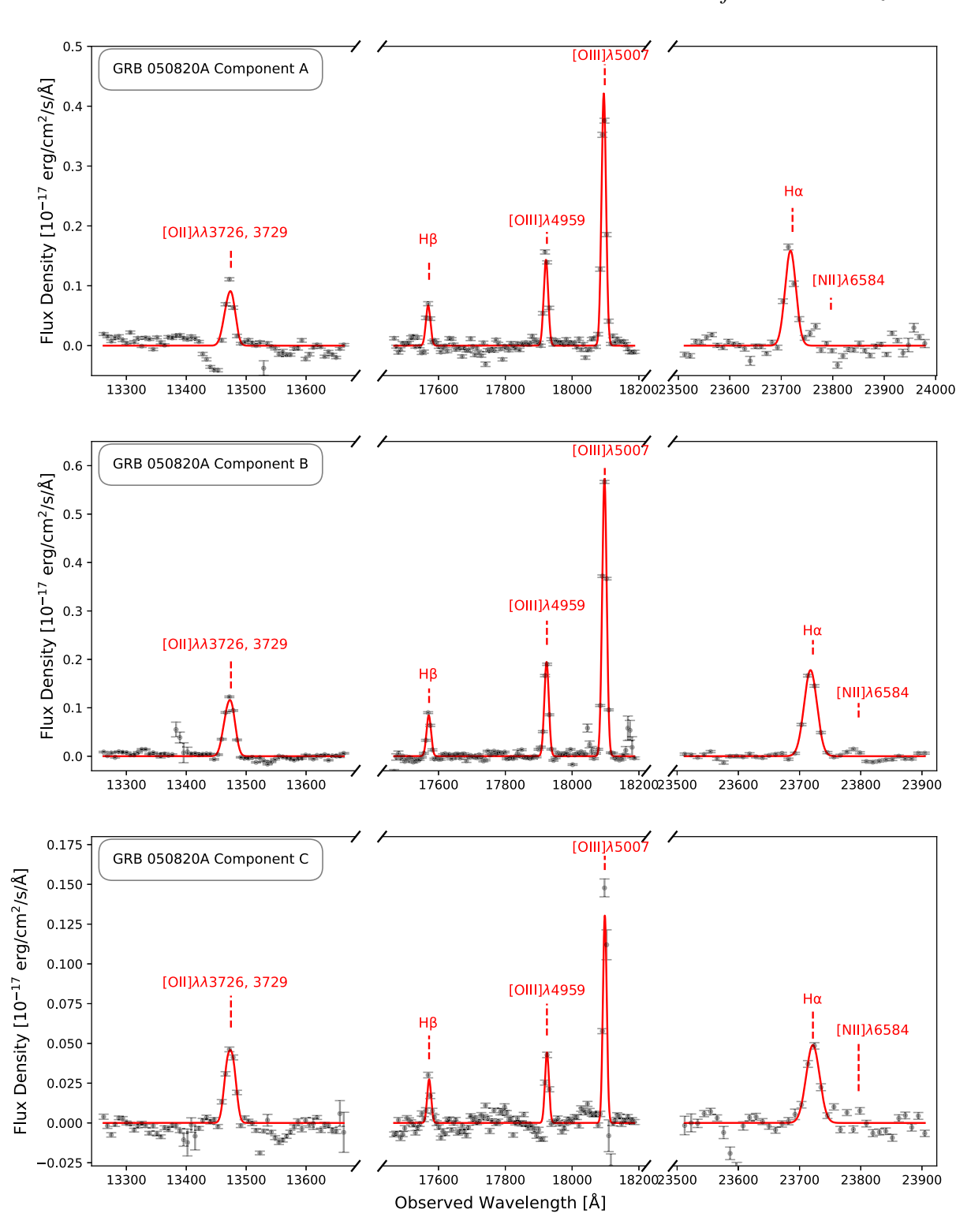


Figure A1. Stacked spectra of all three components of GRB 050820A. The red curves show Gaussian fits to detected emission lines, ranging from  $[O II] \lambda \lambda 3726$ , 3729 to  $H\alpha$ . The expected position of the undetected  $[N II] \lambda 6584$  line is also marked in each spectrum. In both cases, the best-fitting background has been subtracted, centring the noise level at zero. *Note*: for component C, the best-fitting amplitude of  $[O III] \lambda 5007$  appears slightly lower than the top data point due to lower limit of its width being constrained by the instrument LSF.

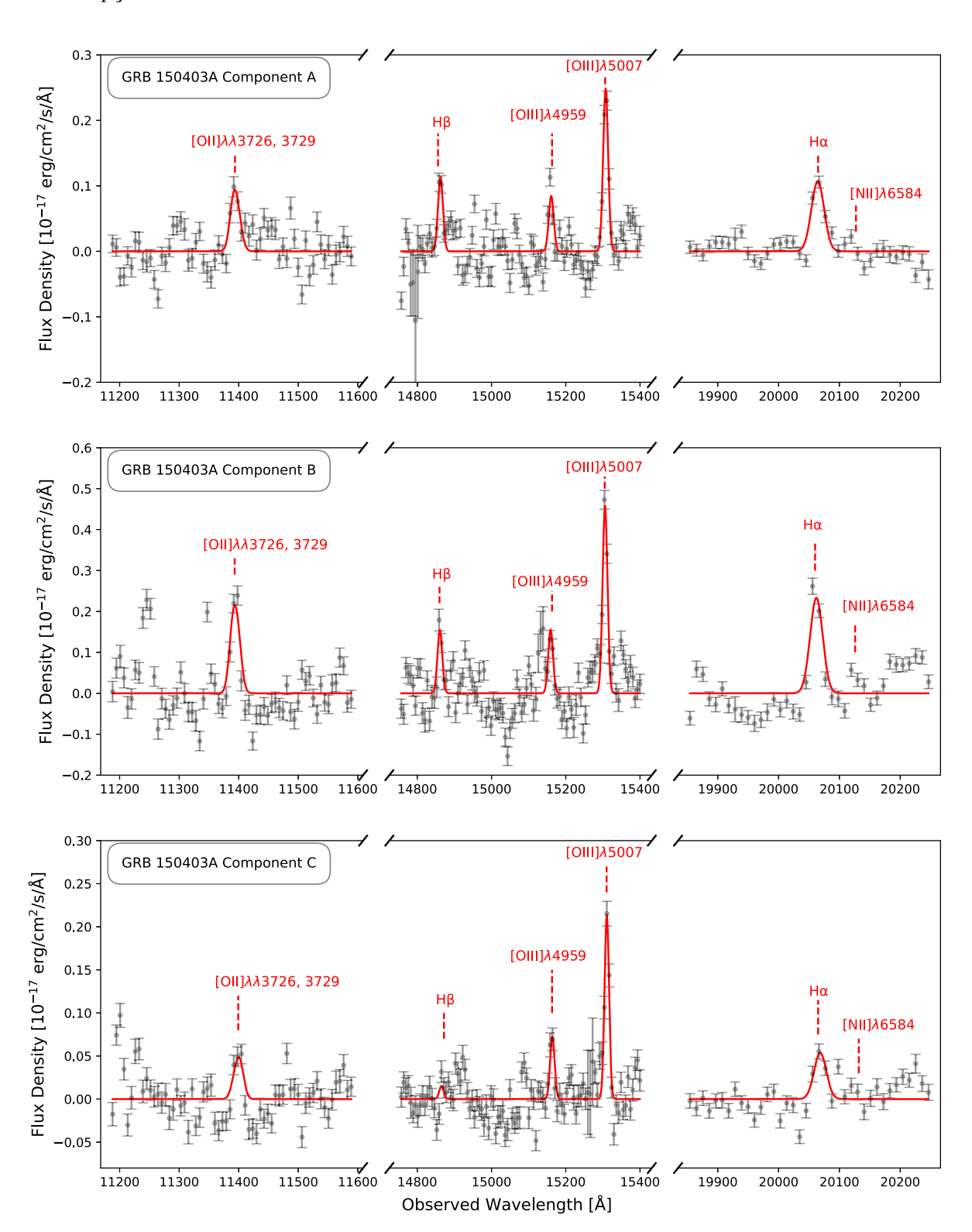


Figure A2. Same as Fig. A1, but for GRB 150403A.

# APPENDIX B: LOWER BRANCH METALLICITIES FROM THE SST24 DIAGNOSTIC

**Table B1.** Table with lower branch SST24  $R_{23}$  (Sanders et al. 2024) emission-line metallicities along with the corresponding  $R_{23}$  line ratios that we measure for the total integrated and individual components detected in the host galaxies of GRB 050820A and GRB 150403A.

GRB host	R <sub>23</sub>	$12 + \log(\text{O/H})$ SST24 $R_{23}$	
050820A			
Total integrated	$1.04 \pm 0.07$	$7.91 \pm 0.19$	
Component A	$1.02 \pm 0.12$	$7.79 \pm 0.28$	
Component B	$1.02 \pm 0.10$	$7.82 \pm 0.27$	
Component C	$0.96 \pm 0.27$	$7.58 \pm 0.45$	
150403A			
Total integrated	$0.96 \pm 0.87$	$7.35 \pm 0.78$	
Component A	$0.62 \pm 0.09$	$6.95 \pm 0.13$	
Component B	$0.80 \pm 0.11$	$7.26 \pm 0.24$	
Component C	$1.77\pm1.71$	< 8.35	

This paper has been typeset from a TEX/LATEX file prepared by the author.